A Novel Robust Kernel Principal Component Analysis for Nonlinear Statistical Shape Modeling from Erroneous Data

Jingting Ma[a,*], Anqi Wang[c], Feng Lin[a], Stefan Wesarg[c], Marius Erdt[a,b]

[a]*Nanyang Technological University, Nanyang Avenue 50, Singapore 639798, Singapore*
[b]*Fraunhofer Singapore, Nanyang Avenue 50, Singapore 639798, Singapore*
[c]*Fraunhofer IGD, Darmstadt 64283, Germany*

Abstract

Statistical Shape Models (SSMs) have achieved considerable success in medical image segmentation. A high quality SSM is able to approximate the main plausible variances of a given anatomical structure to guide segmentation. However, it is technically challenging to derive such a quality model because: (1) the distribution of shape variance is often nonlinear or multi-modal which cannot be modeled by standard approaches assuming Gaussian distribution; (2) as the quality of annotations in training data usually varies, heavy corruption will degrade the quality of the model as a whole. In this work, these challenges are addressed by introducing a generic SSM that is able to model nonlinear distribution and is robust to outliers in training data. Without losing generality and assuming a sparsity in nonlinear distribution, a novel Robust Kernel Principal Component Analysis (RKPCA) for statistical shape modeling is proposed with the aim of constructing a low-rank nonlinear subspace where outliers are discarded. The proposed approach is validated on two different datasets: a set of 30 public CT kidney pairs and a set of 49 MRI ankle bones volumes. Experimental results demonstrate a significantly better performance on outlier recovery and a higher quality of the proposed model as well as lower segmentation errors compared to the state-of-the-art techniques.

Keywords: Statistical Shape Model, Robust Kernel Principal Component Analysis, Data Corruption, Segmentation

1. Introduction

Statistical Shape Models (Davies et al., 2008; Heimann and Meinzer, 2009) have been employed in various applications of medical image segmentation. Using a set of shape training data, SSMs learn the significant variabilities of the anatomical structure of interest via principal component analysis (PCA). The learned prior knowledge can then be used to effectively boost the performance of segmentations by projecting any distorted input shape to the SSM and constraining it to the most plausible modes of variation. In many practical applications, a high quality model with a good balance of generalization and specificity (Davies et al., 2008) significantly contributes to the final segmentation result. In spite of the considerable success, it is still challenging to create high quality models due to the following challenges:

- *Multi-modal Shape Distributions:* The shape variance of many biological structures does not follow a simple Gaussian distribution. For example, the mean shape of a vertebrae model (Kirschner et al., 2011) is not meaningful as it does not represent any existing vertebra. The same applies to combined shapes with non-uniform structure (cf. Fig. 1-(a)), where linearity and nonlinearity exist simultaneously in a probabilistic distribution. Nonlinear SSMs have been proposed, but existing methods cannot accurately project highly distorted input shapes to the nonlinear shape space in order to remove non-plausible distortion. A high level distortion in input shape, however, is likely to occur with most boundary detection methods.
- *Data Corruption:* There are many factors influencing training data quality. Imaging artifacts, inherent noise in images, non-visible organ boundaries, as well as inter- and intra-subject variance may lead to non-ideal delineations which in turn degrade the quality of SSMs using these delineations as training data. Furthermore, in practice, the amount of available ground truth data is usually limited since manual delineation is time-consuming and costly. Severe corruption in training data therefore has a significant impact on the whole SSM.

Addressing these challenges, in this work, a generic SSM framework is proposed that can handle multi-modal shape distribution and at the same time is robust to corrupted data. Another advantage of the proposed model in practice is that its robustness to erroneous data allows for a greater use of non-ideal training data generation methods for statistical shape modeling. For example, semi-automatic seg-

*Corresponding Author.
Email address: jma012@ntu.edu.sg (Jingting Ma)

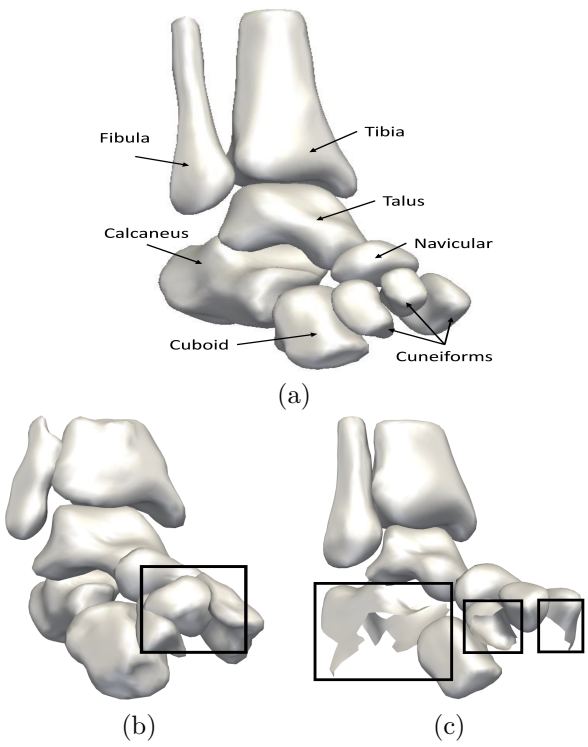

Figure 1: (a) Ankle bone structure (b) Corrupted ankle bone with anomalous overlap marked by a black square (c) Incomplete ankle bone with missing areas marked with black squares

mentation approaches could be used to a greater extent than currently possible to augment the training data base as the proposed SSM framework can still create high quality models in the presence of errors.

Over the past decade, SSMs have been very successful in segmentation tasks which range from organs to lesions, and from soft tissues to hard tissues. In (Soliman et al., 2017), a unified model integrating two appearance sub-models and an adaptive shape sub-model is proposed to segment pathological and healthy lungs. Albà et al. (Albà et al., 2016) present a generic SSM for abnormal hearts segmentation, where the abnormality in patient data is approximated and constrained by back projection onto the SSM. In (Okada et al., 2015; Wilms et al., 2017), SSMs are employed in multi abdominal organ segmentation based on a limited amount of labeled training data. Besides organs, SSM as well as its variations have proven to achieve fairly good results in small region recognition, e.g. brain ROI (Patenaude et al., 2011) and lung with tumors (Sun et al., 2012; Wilms et al., 2012). In addition to the highly deformed soft tissues, segmentation for articulated joints of hard tissue has attracted extensive attention as well. For instance, lumbar vertebrae is an extremely challenging organ for segmentation due to its high complexity in geometry and large variability of individuals. For example, a statistical shape decomposition and conditional model is proposed to overcome such challenges in (Pereañez et al., 2015), where the key technique is to reduce the complexity of subparts and to model inner-relationships. In (Castro-Mateos et al., 2015), an SSM is used to model the inter-space between individuals to avoid overlap for accurate segmentation. In (Rasoulian et al., 2013; Anas et al., 2016), a statistical multi-shape model joint with a pose model is adopted in vertebrae and wrist bone segmentation, respectively. Chen et al. (Chen et al., 2014) build an SSM for wrist bone segmentation incorporating the position variation arising from articulations. Besides the conventional shape model-based segmentation approaches, SSMs are also incorporated with deep neural networks to realize challenging segmentation cases. In (Ma et al., 2018), the SSM is utilized together with the output from deep neural network in a unified framework to achieve the CT pancreas segmentation.

The majority of approaches deal with complex geometry by incorporating other machine learning techniques and/or utilizing integrated shape and pose models under the assumption of a Gaussian-like distribution. In contrast to linear SSMs, the number of approaches exploiting nonlinear variabilities of shape data is relatively small: in (Kirschner et al., 2011), Kernel PCA (KPCA) is leveraged to capture nonlinear variance of SSMs for vertebrae. A recent modeling approach is proposed in (von Tycowicz et al., 2018), which endows a differential representation of shape with a nonlinear Riemannian structure for identification of intra- and inter- population variability. Many biological structures, however, contain nonlinearities even though the non-linearity might not be always strong. In these cases, a linear model does not represent the anatomical structure well. A common approach to deal with non-linearity is to implicitly map the nonlinear data to a much higher dimensional linear feature space with a kernel trick. Examples are KPCA (Mika et al., 1999; Twining and Taylor, 2001), Kernel Support Vector Machines (Kwak, 2013), nonlinear compressive sensing (Qi and Hughes, 2011; Anaraki and Hughes, 2013), and kernelized low rank representation (LRR) (Nguyen et al., 2015; Xiao et al., 2016).

Nevertheless, data corruption is rarely addressed in statistical shape modeling, even though it is one of the most common problems in computer vision. As PCA is sensitive to non-Gaussian outliers, a probabilistic PCA using an EM algorithm is presented in (Lüthi et al., 2009) and applied for statistical shape modeling from corrupt data. Recently, Robust PCA (RPCA) proposed by Candès et al. (Candès et al., 2011), has become a popular trend in statistical shape modeling (Gutierrez et al., 2014; Ma et al., 2016) aiming at handling arbitrarily corrupted data in an unsupervised manner. By recovering a low-rank subspace from training data and filtering our the sparsity, RPCA shows fairly good performance in a wide range of applications from video surveillance to signal processing. Similarly, the low-rank decomposition technique is also applied in pathological liver and lung segmentation in (Shi et al., 2017).

In accordance with the theorem of compressive sensing, we hypothesize that a latent low-rank nonlinear subspace

can be recovered from corrupted training data and a compact shape model is derived from the compressed clean subspace afterwards. This motivates us to perform RPCA on a nonlinear data distribution where the dominant patterns are captured by KPCA. In our previous conference work (Ma et al., 2017) presented at MICCAI 2017, a kernelized RPCA is proposed for creating SSMs where the low-rank modeling is applied on the kernel matrix, which outperforms linear models in coping with corruption in nonlinear data. Expanded from the previous work, in this study, a novel robust KPCA (RKPCA) is proposed with complete mathematical derivations and explanations to construct a low-rank nonlinear feature space from non-ideal training data. It is more generic and robust than the previous approach. Moreover, we compare our RKPCA with another popular RKPCA proposed by Nguyen et al. Nguyen and Torre (2009) that aims to make the pre-image in KPCA robust from a different perspective. We validate our approach on two types of datasets: (1) a public set of 30 kidney pairs aiming at demonstrating the potential of representing nonlinear distributions; (2) a set of 49 corrupted ankle bones consisting of multiple discontinuous subparts representing corruption in a complex geometrical structure.

The rest of the manuscript is organized as follows. In Section 2, we describe the framework of statistical shape modeling and highlight the technical problems of RPCA. In Section 3, we investigate the technical details of KPCA and present our RKPCA approach and its applicability in statistical shape modeling which are the main contributions of this work. In Section 4, experiments are conducted by evaluating the ability of denoising, the quality of several constructed shape models as well as analyzing segmentation results using SSMs on the two test data bases. A conclusion is presented in Section 5.

2. Limitations of Robust Linear SSM

Given a set of N_s training shapes, each of which is represented as a point-set $d_i = \left(x_1, y_1, z_1, \ldots, x_{N_p}, y_{N_p}, z_{N_p}\right)^T$ using the Point Model Distribution (PDM), where N_p indicates the number of landmarks, a column stacked matrix $D = [d_1, \ldots, d_{N_s}]$ is constructed for training a shape model. Afterwards, PCA performs eigen-decomposition on D and extract the first n_k modes of variation from eigenvectors $\{\boldsymbol{\alpha^i}\}_{i:1\ldots n_k}$ and eigenvalues $\Lambda_{i:1\ldots n_k}$ to describe the class of shape. However, PCA is extremely sensitive to non-Gaussian outliers that gives rise to limitations of many applications. Recently, Candès et al. present the RPCA that efficiently addresses the limitation of PCA and achieves satisfactory results in dealing with grossly corrupted data. Taking advantage of the data sparsity, RPCA assumes that the data matrix D can be decomposed into a latent clean low-rank subspace X free of outliers and a sparse component E representing the data sparsity, the objective of which is formulated as

$$\min_{X,E} \|X\|_* + \lambda \|E\|_1 , \quad \text{s.t. } X + E = D, \tag{1}$$

This can be seen as minimizing the nuclear norm $\|X\|_*$, a convex relaxation of minimizing $rank(X)$ (Recht et al., 2010), and l_1 norm with a positive trade-off λ. In (Lin et al., 2010), Lin et al. presented an inexact augmented Lagrange multiplier (IALM) using an additional quadratic penalty in contrast to the standard Lagrange multiplier. We adapt IALM to solve (1) that delivers better performance than the dual approach, proximal gradient and the Exact ALM and formulate the Lagrangian:

$$\begin{aligned}\mathcal{L}(X, E, Y, \mu) = \min_{X,E} \|X\|_* + \lambda \|E\|_1 + \\ \langle Y, D - X - E\rangle + \frac{\mu}{2} \|D - X - E\|_F^2 ,\end{aligned} \tag{2}$$

where Y is multiplier and μ is a positive scalar. The optimization (2) is decomposed into subproblems where $\{X, E, Y, \mu\}$ are iteratively updated in turn, and the order does not affect the optimization. An element-wise soft-thresholding operator $\mathcal{S}_\tau[\cdot]$ (Lin et al., 2010) is introduced for sparsity identification in E and defined as:

$$\mathcal{S}_\tau[X] = \min(X + \tau, 0) + \max(X - \tau, 0), \tag{3}$$

which aims to activate the nonlinearity. With unconcerned variables fixed, a Singular Value Shrinkage (SVS) operator $\mathcal{D}_\tau[\cdot]$ presented in (Cai et al., 2010) is adopted to update X that is defined as:

$$\mathcal{D}_\tau[X] = U\mathcal{S}_\tau[\Sigma]V^T, \quad X = U\Sigma V^T, \tag{4}$$

where $U\Sigma V^T$ is the singular value decomposition (SVD) of X. The idea behind is shrinking the singular values with a pre-defined penalty τ to achieve dimensionality reduction of matrix X. Afterwards, Y and μ are updated with respect to X and E. The procedure is repeated until the Lagrangian optimization converges. Following RPCA, PCA performs eigen-decomposition on the output constructed low-rank component X_L to extract n_k modes of variabilities.

3. Robust Kernel PCA

In this section, we first analyze the technical details of KPCA, which together with RPCA form the basis of our proposed RKPCA. Subsequently, a detailed explanation and derivation of RKPCA is illustrated, the pipeline of which is plotted in Fig. 2.

In KPCA, a kernel trick κ is introduced to establish an implicit mapping Φ from the original shape space to a much higher dimensional feature space $X \rightarrow \Phi(X)$ where PCA is performed afterwards. In this work, we adapt the popular Radial Basis Function (RBF) $\kappa(a, b) = \exp(-\|a - b\|^2 / (2\sigma^2))$ as kernel trick. Given a data matrix X, the gram matrix $K = \mathcal{K}(X)$ is constructed with

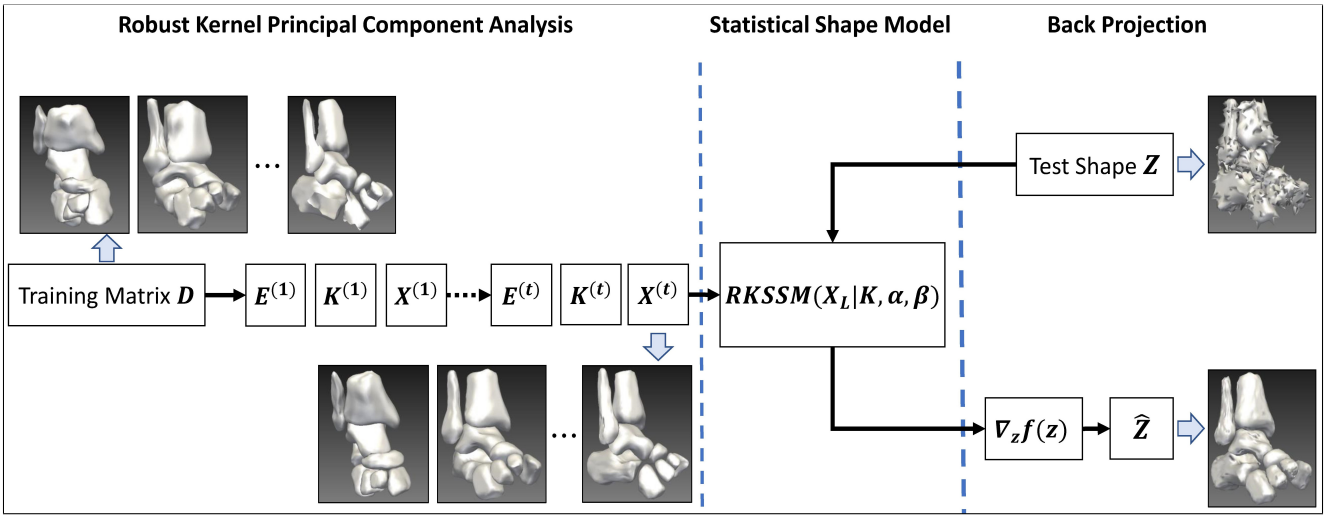

Figure 2: This figure illustrates the pipeline of our RKPCA and the procedure of model back projection: when an unseen shape $\boldsymbol{Z}$ is back projected onto the model, a set of nonlinear principal components are propagated and further used to approximate the reconstruction $\hat{z}$ through the standard pre-image $f(z)$.

each element $K_{ij} = \kappa(x_i, x_j) = \langle \Phi(x_i), \Phi(x_j) \rangle$, where x_i denotes the ith column vector in X. Subsequently, eigen-decomposition is performed on K to extract the first n_k dominant eigenvectors $\boldsymbol{\alpha}$ and eigenvalues Λ instead of carrying out the explicit eigen-decomposition on $\Phi(X)$. Each data point $x_i \in X$ is projected onto a set of nonlinear principal components $\boldsymbol{\beta_i} = \sum_{n=1}^{N_s} \boldsymbol{\alpha_n^{n_k}} \kappa(x_i, x_n)$ with dimension of n_k thereof. Unlike the linear mapping from original data to feature space in PCA, the reverse mapping from kernel space to the original data space is often ill-posed. Mika et al. (Mika et al., 1999) presented a pre-image approach to approximate a shape vector z in the original data space from the kernel space by minimizing:

$$f(z) = \|\Phi(z) - \mathbb{P}_n \Phi(X)\|^2 , \tag{5}$$

where $\mathbb{P}_n \Phi(X)$ denotes projection from the feature space $\Phi(X)$ to the kernel space spanned by nonlinear principal components $\boldsymbol{\beta}$. z is approximated as the stationary point by setting the gradient of (5) zero, which is:

$$\nabla_z f(z) = \sum_{i=1}^{N_s} \gamma_i \frac{\partial}{\partial z} \kappa(x_i, z) = 0, \tag{6}$$

where $\frac{\partial}{\partial z}\kappa(x_i, z)$ denotes the partial derivative of $\kappa(x_i, z)$ with respect to z. Therefore, the approximation point is obtained via:

$$\hat{z} = \frac{\sum_{i=1}^{N_s} \boldsymbol{\gamma}_i \kappa(z, x_i) x_i}{\sum_{i=1}^{N_s} \boldsymbol{\gamma}_i \kappa(z, x_i)}, \quad \gamma_i = \sum_{k=1}^{n_k} \boldsymbol{\beta_k} \boldsymbol{\alpha_i^k}. \tag{7}$$

3.1. Objective formulation

To seek a low-rank component X that is free of outliers and represents primary nonlinear patterns, a straight forward solution is to decompose the high-dimensional feature space by minimizing $\|\Phi(X)\|_* + \lambda \|\Phi(E)\|_1$, which is in favor of the arguments in RPCA (cf. (1)). However, the implicitness of Φ makes it infeasible to determine the stationary point of $\|\Phi(E)\|_1$, as the l_1 norm is an element-wise nonlinear activation. To address this issue, a straightforward way would be minimizing $\|\Phi(X)\|_* + \lambda \|E\|_1$. However, since $\Phi(X)^T \Phi(X) = \mathcal{K}(X)$, $\|\mathcal{K}(X)\|_*$ can be considered to act as surrogate of $\|\Phi(X)\|_*$ because minimizing $\|\Phi(X)\|_*$ is equivalent to minimizing $tr\big((\Phi(X)^T\Phi(X))^{1/2}\big) = tr\big(\mathcal{K}(X)^{1/2}\big)$. Moreover, seeking the optimal $\|\mathcal{K}(X)\|_*$ alleviates computational complexity and its feasibility has been demonstrated in our previous conference work (Ma et al., 2017), where the data matrix decomposition is performed on the gram matrix $\mathcal{K}(X)$. A similar idea of minimizing the rank of the gram matrix is also presented in (Zhang et al., 2016; Wu and Wang, 2017).

Therefore, we aim to seek the best rank of $\mathcal{K}(X)$ instead of explicitly carrying out the unknown dimensional feature space $\Phi(X)$ and present the objective function:

$$\min_{X,E} \ \|\mathcal{K}(X)\|_* + \lambda \|E\|_1 , \quad \text{s.t. } X + E = D. \tag{8}$$

IALM is employed to form the objective Lagrangian:

$$\begin{aligned} \mathcal{L}(X, E, Y, \mu) = \min_{X,E} \|\mathcal{K}(X)\|_* + \lambda \|E\|_1 + \\ \langle Y, D - X - E \rangle + \frac{\mu}{2} \|D - X - E\|_F^2 , \end{aligned} \tag{9}$$

which is solved under an iteration scheme.

3.2. Updating $E^{(t+1)}$

With the unconcerned variables $\{X, Y, \mu\}$ fixed, the Lagrangian $\min_E \mathcal{L}(E, Y, \mu)$ with respect to the sparse component E is written as:

$$\min_E \lambda \|E\|_1 + \frac{\mu}{2} \left\| E - \left(D - X^{(t)} + \frac{1}{\mu} Y \right) \right\|_F^2 ,$$

and E is updated by introducing the soft-thresholding operator (3) that:

$$E^{(t+1)} = \mathcal{S}_{\frac{\lambda}{\mu^{(t)}}}\Big[D - X^{(t)} + \frac{1}{\mu^{(t)}}Y^{(t)}\Big], \tag{10}$$

where t indicates the iteration that starts from 0.

3.3. Updating $K^{(t+1)}$

We arrive at optimization to X based on the updated $E^{(t+1)}$, the Lagrangian $\mathcal{L}(X, Y, \mu)$ with respect to X is given by:

$$\min_X \|\mathcal{K}(X)\|_* + \frac{\mu}{2}\left\|X - \Big(D - E^{(t+1)} + \frac{1}{\mu}Y\Big)\right\|_F^2. \tag{11}$$

It is infeasible to directly apply the singular value shrinkage $\mathcal{D}_\tau[\cdot]$ to the Lagrangian, which brings difficulty to giving the optimal $X^{(t+1)}$. Hence, we decompose the optimization (11) into two subproblems with respect to X at each iteration. Specifically, we consider X a constant to seek the optimal rank of the gram matrix $\mathcal{K}(X)$. We subsequently derive $X^{(t+1)}$ with the obtained $\boldsymbol{K^{(t+1)}}$ by reaching the sub-stationary point:

$$\begin{cases} \boldsymbol{K^{(t+1)}} = \min\limits_{\mathcal{K}(X)} \|\mathcal{K}(X)\|_* \\ \boldsymbol{X^{(t+1)}} = \min\limits_X \mathcal{K}(X) + \frac{\mu}{2}\left\|X - \Big(D - E^{(t+1)} + \frac{1}{\mu}Y\Big)\right\|_F^2 \end{cases}$$

The Lagrangian (11) is separable because the nuclear norm and Frobenius norm are both convex.

To achieve dimensionality reduction for outlier removal, at this stage, we apply the low-rank modeling to the gram matrix, which is similar to the objective function in our previous conference work (Ma et al., 2017) and formulated as:

$$\min_K \left\|\boldsymbol{K^{(t)}}\right\|_*, \quad \text{s.t. } \boldsymbol{K^{(t)}} = \mathcal{K}\Big(D - E^{(t+1)}\Big). \tag{12}$$

It is a special case of matrix decomposition denoted as matrix completion in (Cai et al., 2010). Associated with a Lagrange multiplier A, the low-rankness of gram matrix is promoted iteratively by

$$\begin{cases} K^{(u+1)} = \mathcal{D}_{\mu_k}\Big[\boldsymbol{K^{(t)}} + \frac{1}{\mu_k}A^{(u)}\Big] \\ A^{(u+1)} = A^{(u)} + \mu_k\Big(\boldsymbol{K^{(t)}} - K^{(u+1)}\Big) \end{cases} \tag{13}$$

where u decides the iteration, and $\{K^{(u+1)}, A^{(u+1)}\}$ are optimal solutions in each iteration and initialized as $K^{(0)} = \mathcal{K}(D - E^{(t+1)})$ and $A^{(0)} = 0$ respectively. It should be pointed out that the sought of low-rank $\boldsymbol{K^{(t)}}$ is an inner loop embedding in the whole RKPCA optimization. The procedure of low-rank modeling will converge to an accumulation point where $\left\|\boldsymbol{K^{(t)}} - K^{(u+1)}\right\|_F / \left\|\boldsymbol{K^{(t)}}\right\|_F \leq \epsilon_k$, a theoretical guarantee is provided in (Candès and Recht, 2009). Until the convergence condition for the inner loop is satisfied, we simply take the final output and denote $\boldsymbol{K^{(t+1)}} = K^{(u+1)}$, which may not be symmetrical and full-rank. In this manner, $\|\mathcal{K}(X)\|_*$ is solved and the updated $\boldsymbol{K^{(t+1)}}$ is then applied to derive $X^{(t+1)}$.

3.4. Updating $X^{(t+1)}$

For the ease of presentation, we denote the constant $C = \mu/2\big(D - E^{(t+1)} + 1/\mu Y\big)$. Denote $\rho(X) = \mathcal{K}(X) + \mu/2\,\|X - C\|_F^2$, $X^{(t+1)}$ is optimized by deriving the subgradient of $\rho(X)$ and assumed to be the stationary point. The subgradient of $\rho(X)$ is defined as:

$$\frac{\partial}{\partial X}\rho(X) = \frac{\partial}{\partial X}\mathcal{K}(X) + \frac{\partial}{\partial X}\frac{\mu}{2}\|X - C\|_F^2. \tag{14}$$

The partial derivative of frobenius norm is easily obtained by:

$$\frac{\partial}{\partial X}\frac{\mu}{2}\|X - C\|_F^2 = \mu\big(X - C\big). \tag{15}$$

Subsequently, we seek the partial derivative of $\mathcal{K}(X)$ with respect to X. As opposed to the standard pre-image in (5) which also aims to approximate the projections from gram matrix to the input space, we leverage the value of low-rank $\boldsymbol{K^{(t+1)}}$ straightforwardly, implying the new affinities between data point, instead of using any principal components derived from eigen-decomposition. Theoretically, computing the derivative of Matrix-by-Matrix can be accomplished by vectorizing the denominator matrix so that the Kronecker product will be leveraged to approximate the derivatives of Matrix-by-Scalar. However, this will raise the computational complexity on account of the large dimensionality in the derivative matrix. Moreover, the Kronecker product might cause high sparsity because each element K_{ij} in the gram matrix is only related to x_i and x_j but not to all the members. Addressing this issue, we present a novel solution to the partial derivative of $\partial_X\mathcal{K}(X)$ that is defined as:

$$\frac{\partial}{\partial X}\mathcal{K}(X) = \begin{bmatrix} \frac{\sum_{i=1}^{N_s}\partial\kappa(x_i,x_1)}{\partial X_{11}} & \cdots & \frac{\sum_{i=1}^{N_s}\partial\kappa(x_i,x_{N_s})}{\partial X_{1N_s}} \\ \vdots & \ddots & \vdots \\ \frac{\sum_{i=1}^{N_s}\partial\kappa(x_i,x_1)}{\partial X_{3N_p1}} & \cdots & \frac{\sum_{i=1}^{N_s}\partial\kappa(x_i,x_{N_s})}{\partial X_{3N_pN_s}} \end{bmatrix} \tag{16}$$

More specifically, we sum up all the derivatives related to X_{ij} in order to avoid the sparsity caused by the Kronecker product.

Substituting (15) and (16) into (14) and set it to zero, thus we have:

$$\sum_{n=1}^{N_s}\boldsymbol{K_{nj}^{(t+1)}}X_j^{(t)} - \sum_{n=1}^{N_s}\boldsymbol{K_{nj}^{(t+1)}} + \mu X_j^{(t)} - \mu C_j = 0, \tag{17}$$

where j indicates each column in X and C, namely, $X^{(t+1)}$ is computed in column-by-column. Therefore, we come to the final solution:

$$X^{(t+1)} = \sum_{j=1}^{N_s}\frac{\mu C + \sum_{n=1}^{N_s}\boldsymbol{K_{nj}^{(t+1)}}X_j}{\mu + \sum_{n=1}^{N_s}\boldsymbol{K_{nj}^{(t+1)}}}. \tag{18}$$

3.5. Convergence analysis

Based on the updated $X^{(t+1)}$ and $E^{(t+1)}$, we update the multiplier $Y^{(t+1)} = Y^{(t)} + \mu^{(t)}\big(D - X^{(t+1)} - E^{(t+1)}\big)$. Positive scalars μ and μ_k are updated exactly in the same way that $\mu^{(t+1)} = \min\big(\mu^{(t)}(1+\eta), \bar{\mu}\big)$, and $\mu_k^{new} = \min\big(\mu_k^{old}(1+\eta), \bar{\mu_k}\big)$. Analogous to the inner loop (13), sequence $\{X, E, Y, \mu\}$ converges when $\left\|D - X^{(t+1)} - E^{(t+1)}\right\|_F / \|D\|_F \leq \epsilon$. In this way, a low-rank component X_L is recovered from the original data D where outliers are discarded and KPCA is performed to extract nonlinear principal components $\boldsymbol{\beta}$ and corresponding eigenvectors $\boldsymbol{\alpha}$ for statistical shape modeling.

We summarize the whole procedure of statistical shape modeling using the proposed RKPCA in Alg. 1.

Algorithm 1 Nonlinear statistical shape modeling via RKPCA

Input: training matrix D.
Initialize: $Y^{(0)}, \mu^{(0)}, \mu_k^{(0)}, t = 0$.

while not converged **do**
  Update $E^{(t+1)}$ via (10)
  Update $\boldsymbol{K^{(t)}} \leftarrow \mathcal{K}\big(D - E^{(t+1)}\big)$
  Initialize: $A^{(0)} = 0, K^{(0)} = \boldsymbol{K^{(t)}}, u = 0$.

  while not converged **do**
    Update $\{K^{(u)}, A^{(u)}, \mu_k^{(u)}\}$ via (13)
    $u = u + 1$
  end while

  Output: $\boldsymbol{K^{(t+1)}} = K^{(u+1)}$
  Update $X^{(t+1)}$ via (18)
  Update $Y^{(t+1)}, \mu^{(t+1)}$
  $t = t + 1$
end while

Perform KPCA on the recovered low-rank matrix X_L.
Output: $RKSSM(X_L|K, \boldsymbol{\alpha}, \boldsymbol{\beta})$.

3.6. Computational complexity analysis

Regarding the computational complexity of the proposed RKPCA, we denote $m = 3N_p$ and $n = N_s$ as the dimension of training matrix for ease of presentation. In each iteration, the main computational cost comes from (1) computation of gram matrix with $\mathcal{O}(mn^2)$ time complexity, (2) singular value shrinking the updated gram matrix from (13) that takes $\mathcal{O}(n^3)$ and (3) the partial derivative to update X from (14), which takes $\mathcal{O}(dmn)$. Overall, the time complexity of Algorithm 1 for one iteration is $\mathcal{O}(mn^2 + n^3)$. In contrast to the competitive linear approaches, the main computational complexity of PCA is from the covariance matrix and eigen-decomposition, i.e. $\mathcal{O}(m^2n + n^3)$, which of RPCA comes from the SVD with $\mathcal{O}(\min(mn^2, m^2n))$. Regarding the other nonlinear modeling techniques, the computational complexity is contributed by the gram matrix computation as well as eigen-decomposition and/or SVD, and approximately measured as $\mathcal{O}(mn^2 + n^3)$. That is to say, our RKPCA does not have much more computational cost when $n \ll m$.

4. Evaluation

Our method is evaluated on two representative datasets involving a set of kidney pairs and a set of ankle bones with arbitrary erroneous data. The results are compared with five closely pertinent approaches: conventional **PCA**, **RPCA** (Candès et al., 2011), **KPCA** (Mika et al., 1999), **NIPS-09** (the robust KPCA approach (Nguyen and Torre, 2009)) and our previous conference work **MICCAI-17** (Ma et al., 2017). Even though KPCA is not bounded by pre-image approaches, we choose the popular pre-image strategy presented by Mika et al. (Mika et al., 1999) in this work. In Nguyen and Torre (2009), Nguyen et al. present a Robust KPCA approach consisting of a nonlinear principal components extraction as described in KPCA and a robust pre-image. In contrast to the objective in (5), the reconstruction $\Phi(z)$ of NIPS-09 is required to be close to $\mathbb{P}_n\Phi(z)$ as well as the input sample with a balance trade-off constant ω, of which the objective is formed as $\min_z \|\Phi(x) - \Phi(z)\|_2^2 + \omega \|\Phi(z) - \mathbb{P}_n\Phi(z)\|_2^2$.

First, experiments are conducted to evaluate the ability of dealing with arbitrarily erroneous data and missing areas for competitive methods. Furthermore, we create SSMs using all these methods and evaluate the quality of the resulting models as well as the accuracy of segmentation using these SSMs.

4.1. Datasets

To investigate the ability for representing the nonlinear patterns of the competitive approaches, we create a kidney SSM with each pair consisting of the left and right kidney (cf. Fig. 8). Despite that each single kidney (left/right) follows a linear distribution, the restricted inner space between two single kidneys brings nonlinearity to the whole, which is exactly the reason for choosing the data. 30 public CT datasets are collected from MICCAI 2015 Challenge Multi-Atlas (Landman et al., n.d.), with volume sizes varying from 512 × 512 × 85 to 512 × 512 × 198, the slice thickness varying from 2.5 to 5.0 mm and in-plane resolution varying from 0.54 mm to 0.98 mm. Moreover, we utilize 49 internal MRI ankle bone datasets where each ankle bone consists of 9 discontinuous subparts with narrow inner space (cf. Fig. 1-(a)) to validate our approach on corrupted training data with a complex geometrical structure. The volume size varies from 384 × 384 × 147 to 512 × 512 × 139 and the voxel size ranges from 0.46 × 0.46 × 0.50 mm^3 to 0.49 × 0.49 × 0.50 mm^3. Patients were 20 females and 29 males with age interval of 13 to 17 years.

For resolution consistency, kidney images with ground truth are rescaled to iso-cubic volumes with dimension

$256 \times 256 \times 256$ and the MRI ankle images as well as ground truth are rescaled to $512 \times 512 \times 128$. Then, we obtain training shapes by extracting polygon meshes from the binary ground truth through Marching Cubes. As it is known that a crucial step before modeling is creating a groupwise correspondence among all training shapes for statistics analysis. We employ the point-to-point correspondence approach presented in (Kirschner and Wesarg, 2010), in order to assign the same order of landmarks to areas with similar features. For the kidney datasets, we establish correspondence to the left and right kidneys respectively and merge both afterwards. As a result, each kidney pair contains 4000 landmarks. Similarly, the same correspondence approach is employed respectively to each subpart of ankle, e.g. Fibula and Tibia, hence a whole merged shape of ankle bone consists of 5148 landmarks in total. Subsequently, the training shapes with correspondence are centered at the origin and aligned via rigid Procrustes alignment.

4.2. Parameters

Generally speaking, the low-rank modeling techniques have compelling advantages of being light weight and trained unsupervised compared to the recent trend deep neural networks. Even though a number of parameters and variables are leveraged in our technique, most of them are tuned related to the training data following certain rules. Table 1 shows the parameters and descriptions that are used in RKPCA. It should be pointed out that the trade-off λ, initialization for multiplier Y, μ, μ_k, and the update rate η are all chosen according to the work (Lin et al., 2010), where $\|D\|_2$ decides the l_2 norm of matrix D and $\|D\|_\infty$ denotes the maximum absolute value of the matrix entries.

Table 1: Parameters and Descriptions

Parameter	Description	Value
λ	trade-off in (8)	$\frac{1}{\sqrt{\max(N_s, 3N_p)}}$
$Y^{(0)}$	the initial Lagrange multiplier	$\frac{D}{\min\left(\|D\|_2, \lambda^{-1}\|D\|_\infty\right)}$
η	update rate of μ and μ_k	1.6
$\mu^{(0)}$	the initial value of μ	$1.25/\|D\|_2$
$\bar{\mu}$	maximum of μ	10^5
ϵ	terminate value	10^{-6}
$\mu_k^{(0)}$	the initial value of μ_k	$1.25/\|\boldsymbol{K}\|_2$
$\bar{\mu_k}$	maximum of μ_k	10^5
ϵ_k	terminate value	10^{-3}

It remains to discuss the kernel width σ in RBF trick that has a vital effect on the underlying degree of the model. Specifically, a large width reduces the difference between any two data points leading to a compact feature space, while a small width enlarges this difference leading to a model with large variabilities. Essentially, a small sigma preserves the features while a large sigma is a better choice for larger dimensionality reduction. To keep consistency with other works, the kernel width σ is computed by:

$$\sigma = \frac{1}{2N_s^2} \sum_{i=1}^{N_s} \sum_{j=1}^{N_s} \delta(x_i, x_j), \tag{19}$$

where $\delta(x_i, x_j) = \|x_i - x_j\|$ is the average symmetric distance (ASD) between the shape x_i and x_j.

4.3. RKPCA for Outlier Recovery

As aforementioned, erroneous data are often arbitrarily distributed across the training samples and our proposed RKPCA is supposed to construct approximately the same subspace from a corrupted training dataset as that from an uncorrupted one. Under this assumption, experiments are conducted to assess the ability of outlier recovery for competitive methods. We artificially make the ground truth datasets corrupted and compare the distances between the reconstruction of corrupted training data (cf. Fig. 2, X_L denotes the reconstruction in our RKPCA) and its corresponding ground truth, i.e. smaller distance indicate higher accuracy of outlier recovery. To be specific, a proportion of landmarks of all the training shapes are removed at once, which makes the training data matrix contain arbitrarily distributed missing entries. Through varying the amount of landmark removal, we have training datasets that are corrupted to varying degree thereof. In the experiments, (1) the removing entries are randomly selected per training shape and are different throughout the population; (2) all the missing entries are set to the same point, however, this location is not restricted and in general it does not effect the outlier recovery results; (3) both datasets of kidney pair and ankle bone are employed in the outlier recovery evaluation, where the ground truth shapes are used as the training datasets. We illustrate the results for kidney pairs for more intuitive comparison.

Since the kidney pairs are pre-centralized, a proportional of points are randomly removed from the original datasets and these 3D coordinates are set to the origin, the corresponding triangulation connectivities are changed thereof (cf. Fig. 3 and Fig. 4). Table 2 reports the symmetrical distance between the reconstructed shapes and corresponding ground truth with corruption degrees ranging from 0% to 50%. The kernel width σ is chosen as 473.33, 1062.33, 1327.75, 1484.77, 1579.65, 1631.16 in cases where the proportion of removed landmarks is 0%, 10%, 20%, 30%, 40% and 50% respectively. The paired t-test under null hypothesis is used as the test statistic to decide whether the results are statistically significant. Fig. 3 and Fig. 4 intuitively illustrate the comparisons of ground truth and reconstructions from competitive methods, where the corruption degrees are set to 20% and 40% respectively.

Correspondingly, Table 3 reports the computation time in application (in second) on **Intel** Core i7 processor. With

Table 2: Reconstruction errors (mm) of kidney pairs for different methods and proportion of missing values. The star $*$ indicates a statistically significant difference between the corresponding results and our method at a significance level $\alpha = 0.01$.

	0%	10%	20%	30%	40%	50%
PCA	2.451 ± 0.380*	16.974 ± 4.947*	28.174 ± 6.572*	35.898 ± 6.691*	40.994 ± 7.265*	45.330 ± 8.084*
RPCA	3.302 ± 1.246*	**5.797 ± 1.932**	9.650 ± 5.182*	13.862 ± 2.188*	20.177 ± 2.665*	32.176 ± 3.603*
KPCA	5.523 ± 5.831*	17.938 ± 4.593*	24.404 ± 6.979*	32.273 ± 7.616*	39.718 ± 8.931*	44.962 ± 9.869*
NIPS-09	2.668 ± 12.735*	18.430 ± 4.002*	21.778 ± 5.004*	27.454 ± 7.308*	37.932 ± 3.950*	45.450 ± 8.709*
MICCAI-17	2.985 ± 1.463*	9.181 ± 2.576*	10.844 ± 2.648*	13.217 ± 3.168*	18.552 ± 2.970*	20.639 ± 2.903*
RKPCA	**2.050 ± 0.392**	6.310 ± 1.330	**8.702 ± 1.863**	**10.648 ± 2.339**	**14.032 ± 3.017**	**18.534 ± 2.692**

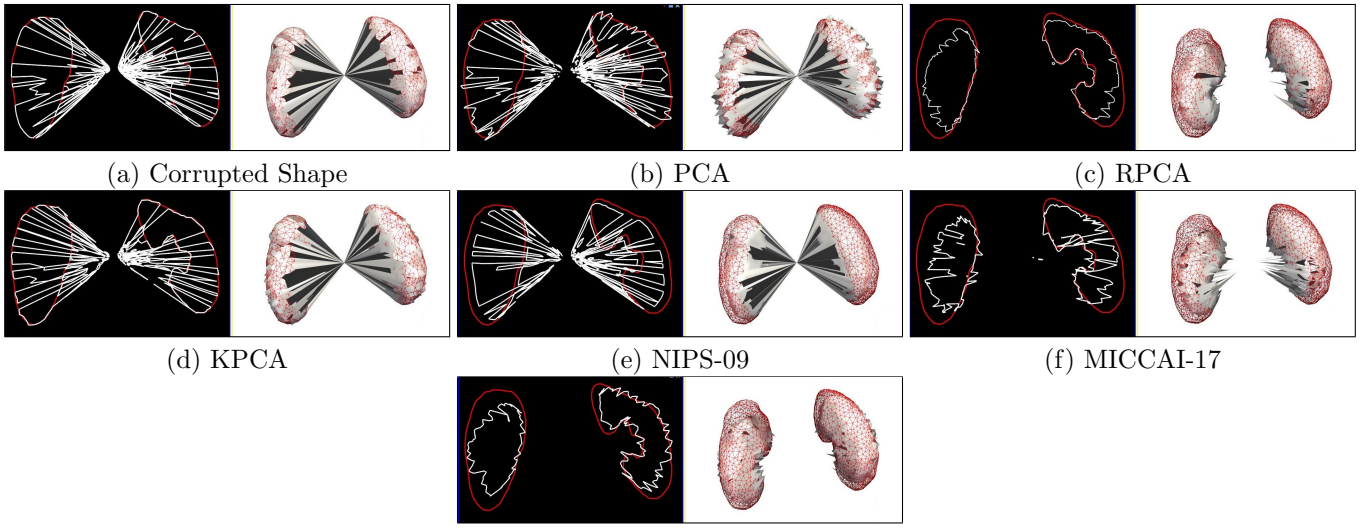

(a) Corrupted Shape (b) PCA (c) RPCA

(d) KPCA (e) NIPS-09 (f) MICCAI-17

(g) RKPCA

Figure 3: The figure plots a corrupted shape (a) with its reconstructions from competitive models (b) - (g) illustrated from the perspective of Coronal-Axial view (left) and 3D rendering (right), where the red shape indicates the ground truth. (a) is artificially generated with 20% of landmarks randomly removed.

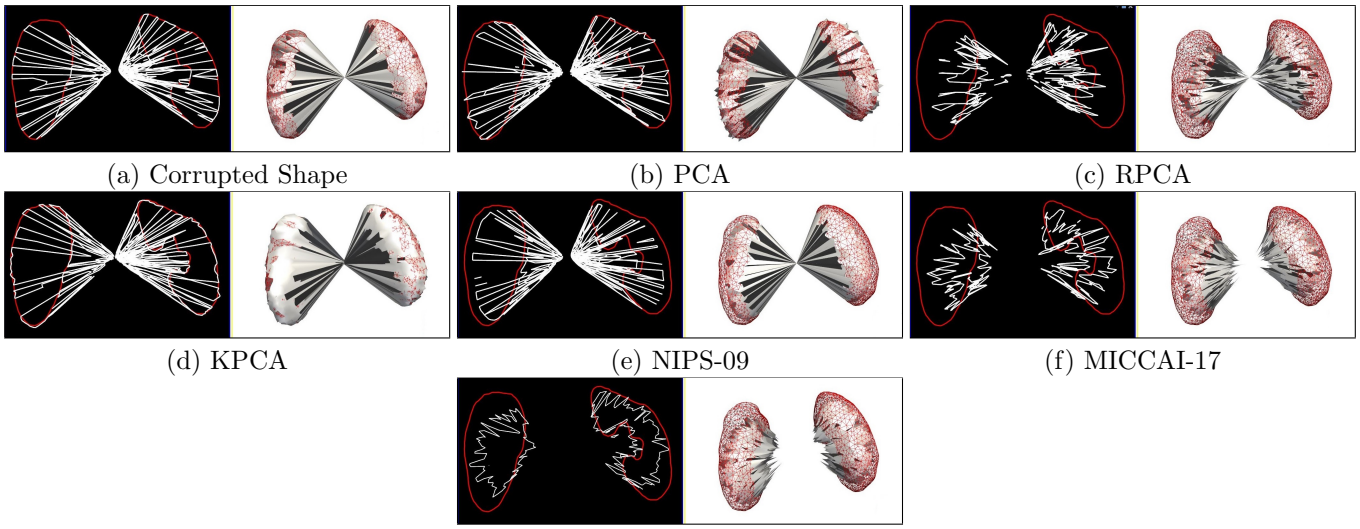

(a) Corrupted Shape (b) PCA (c) RPCA

(d) KPCA (e) NIPS-09 (f) MICCAI-17

(g) RKPCA

Figure 4: The figure plots a corrupted shape (a) with its reconstructions from competitive models (b) - (g) illustrated from the perspective of Coronal-Axial view (left) and 3D rendering (right), where the red shape indicates the ground truth. (a) is artificially generated with 40% of landmarks randomly removed.

the increase of proportion of missing entries, the number of convergence iteration also increases in the nonlinear subspace compression in our RKPCA and the pre-image in other methods. Table 4 reports the computation time with respect to the scale of training data matrix $D \in \mathbb{R}^{m \times n}$, where the first row indicates the results for kidney pair reconstruction and the second row indicates the results for ankle bone reconstruction.

Table 3: The computation time (s) for reconstruction of kidney pairs with various proportion of missing values from 0% to 50% for different methods.

Method	0%	10%	20%	30%	40%	50%
PCA	1.846	1.632	1.465	1.791	1.257	1.641
RPCA	2.936	2.927	2.497	2.378	2.759	2.134
KPCA	12.340	36.120	56.120	99.150	60.720	35.520
NIPS-09	13.510	14.312	15.043	15.248	16.309	16.151
MICCAI-17	3.800	7.181	16.520	30.900	45.900	26.920
RKPCA	**2.152**	**2.610**	**2.923**	**3.105**	**3.502**	**3.370**

Table 4: The computation time (s) for reconstruction of kidney pairs (first row) and ankle bones (second row) using RKPCA with various proportion of missing values from 0% to 50%, where m, n denote the scale of data matrix.

m	n	0%	10%	20%	30%	40%	50%
12000	30	2.152	2.610	2.923	3.105	3.502	3.370
15444	49	5.190	6.331	5.253	6.320	7.534	5.250

Conclusions can be drawn from Table 2. First of all, RPCA, MICCAI-17 and our RKPCA all have the ability to deal with arbitrary outliers. Particularly, RPCA outperforms in cases of small corruption, whereas, RKPCA shows significantly better performance when the corruption degree becomes higher and the power of RPCA degrades (cf. Fig. 3-(c), (g) and Fig. 4-(c), (g)). This is mainly because RKPCA exploits the affinities of each pair of training data across the population and RPCA exploits the variance for every dimension individually. RPCA offers a finer reconstruction compared to RKPCA when the training data is slightly corrupted. However, when the corruption degree becomes higher, the number of reliable variables in each dimension is reduced, which makes it theoretically difficult to learn the dominant variability. In contrast, RKPCA is still capable to exploit the primary nonlinear patterns because the impact of outliers is alleviated during the kernelizing. Secondly, the reason for the reconstruction error with none missing values is that, all the modeling techniques are based on dimensionality reduction in accordance with compressive sensing where usually 95% variabilities are retained. Moreover, NIPS-09 delivers slightly better results than KPCA but obviously worse results than the RKPCA. This is mainly because NIPS-09 is not robust to unknown arbitrary erroneous data across the training population. In terms of the intuitive comparison illustrated in Fig. 3 and Fig. 4, where we find the competitive models eliminate corruptions to different extent but our RKPCA delivers the best reconstruction quality overall.

4.4. RKPCA for Missing Area Completion

Besides the erroneous points, training shapes are often incomplete with missing parts in realistic applications. Therefore, experiments are conducted to assess the ability of missing areas completion. Assume that the missing areas are arbitrarily distributed across the whole shape, a subset of landmarks are randomly selected and removed together with their neighboring landmarks (cf. Fig. 5). In this manner, we artificially make all the ground truth datasets incomplete and aim to assess the reconstruction accuracy, namely, closer to the corresponding ground truth data indicates higher accuracy. In this set of experiments, about 15 landmarks are randomly selected from each training shape and all the incomplete shapes are different across the population. Through varying the area of neighborhood around these selected landmarks, we thus generate training shapes with different degree of incompleteness (cf. Fig. 6), which is considered as the ratio between the sum of missing points and the total number of landmarks.

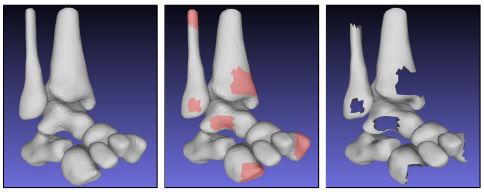

(a) (b) (c)

Figure 5: This figure plots the procedure of incomplete shapes generation: based on a ground truth shape (a), several pieces with varying areas are randomly selected (marked in red in (b)) and removed. An incomplete shape (c) with missing areas is generated thereof.

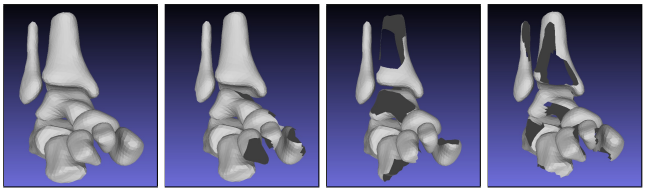

(a) (b) (c) (d)

Figure 6: The figure plots the ground truth ankle bone shape (a) and the artificially generated incomplete shapes with 10%, 20% and 30% removing points in (b), (c) and (d) respectively.

Table 5 reports the reconstruction errors for competitive methods, where the degree of incompleteness varies from 0% to 50%. For an intuitive view, Fig. 7 illustrates the reconstructions of incomplete training shapes with 30% missing areas compared to the ground truth (marked in red). It can be found that the triangulation connectivities are changed due to the removal of landmarks. To be specific, the white pieces in Fig. 7-(a) denote the overlap of

ground truth and incomplete shape, and the missing landmarks are close to the central position because the ankle bones are pre-centralized.

Conclusions can be drawn from Table 5 that RPCA, MICCAI-17 and our proposed RKPCA have much more capability of dealing with missing areas among the competitive methods. With the degree of incompleteness increases, nonlinear approach KPCA performs slightly better than PCA and RKPCA beats RPCA significantly.

4.5. Model Evaluation

After evaluating the performance of the proposed RKPCA, we create SSMs using competitive approaches and assess the model quality where the kidney models are created using the ground truth datasets and the ankle bone models are created using the generated corrupted datasets. Specifically, to make the ankle bone shapes arbitrarily corrupted, we create a SSM with 5 ground truth datasets via PCA and embed it into an existing segmentation framework (Steger et al., 2014) to re-segment the 49 datasets. The idea of the segmentation framework is that each landmark on the surface is deformed in terms of the adaption rules, the whole shape is projected on the model afterwards. Due to the limitation of this segmentation procedure, the segmented shapes may contain corrupted regions to different extent, e.g. the abnormal overlap in Fig. 1-(b). Hereafter, the ankle bone SSMs are all derived based on the generated 49 shapes with arbitrary corruptions, while the ground truth datasets are used for evaluation.

For an intuitive understanding of the robustness to nonlinearity, we compare the shapes generated from the first mode of variance for models derived with RPCA and our RKPCA under the datasets of kidney pair in Fig. 8. It is apparently seen that the shapes generated from RPCA model (cf. Fig. 8-(a) left and right) make no sense in realistic scenarios, where the left kidney is too close to the right kidney. Note that the variance for linear models varies in the range $\left[-3\sqrt{\Lambda_i}, +3\sqrt{\Lambda_i}\right]$, for nonlinear models which varies in the range $\left[-\sqrt{N_s\Lambda_i}, +\sqrt{N_s\Lambda_i}\right]$ as defined in (Twining and Taylor, 2001), where $i = 1 \cdots n_k$. Similarly, the plotting of the first mode of variance for KPCA and RKPCA models shown in Fig. 9, which suggests the robustness to data corruption of the proposed RKPCA. Obviously it is found that the shapes from KPCA model still have erroneous areas, e.g. the overlap (cf. Fig. 9-(a) left) and anomalously deformed subparts (cf. Fig. 9-(a) right), by contrast, our RKPCA model efficiently eliminates the abnormalities in training data.

The most common measures to quantize the quality of SSMs are Generalization ability G, Specificity S and Compactness C provided in (Davies et al., 2008). A model with good generalization is able to represent not only the trained shapes, but also deviations. In contrast to a general model, a specific model represents shapes close to the training data. Thus it does not represent large variances. In addition, a model is compact in case it is capable to describe the model's probability density function (PDF) by a small number of variances. Given a set of N_s training datasets $\{x_i : i = 1 \cdots N_s\}$, we denote a set of M shapes $\{y_A : A = 1 \cdots M\}$ randomly generated from the model's PDF, which approximately covers the whole PDF of the model when $M \to \infty$. G and S are defined as:

$$\begin{cases} G_m = \frac{1}{N_s} \sum\limits_{i=1}^{N_s} \delta(x_i, \tilde{x_i}) \\ S_m = \frac{1}{M} \sum\limits_{A=1}^{M} \min\limits_{i} \delta(y_A, x_i) \end{cases} \tag{20}$$

where m is the number of modes used to generate the samples y_A from the model's PDF. Upon a leave-one-out mode that excluding each of training shapes x_i in turn and then project it onto the model derived with the remaining datasets Davies et al. (2008), G is measured as the distance between x_i and its reconstruction $\hat{x_i}$ thereof. Lower value of G implies smaller distance between the training data points and generated samples, namely, a better performance of generalization ability. On the other hand, S measures the distance from all generated samples to the closest training data. Smaller values of S indicate the model is more specific, i.e. a higher quality model. Compactness is computed by $C_m = \sum_{i=1}^{m} \Lambda_i / \sum_{i=1}^{n_k} \Lambda_i$, which measures the relative variance learned by the dominant modes, i.e. higher ratio indicates better compactness. We report the G, S and C for the kidney models and ankle bone models in Fig. 10 and Fig. 11 respectively.

To compute specificity, $M = 1000$ shapes in total are randomly drawn from the model PDF. As the models of the ankle bone are derived based on corrupted training data, we compute G and S using corresponding ground truth data $\{x_i\}$ and $\{y_A\}$ generated from model's PDF. Fig. 10 shows that our proposed RKPCA consistently boost the performance of model, in particular, the improvement of specificity suggests the considerable ability in describing nonlinear PDF. On the other hand, Fig. 11 reports a higher quality of RKPCA model in coping with data corruption, especially in terms of generalization ability. It should be pointed out that **KPCA** and **NIPS-09** compute the gram matrix in the exact same way, resulting in the equivalent eigenvalues $\Lambda_{i:1\cdots n_k}$.

4.6. Segmentation Evaluation

To assess the effect on segmentation accuracy, the derived SSMs are used in two existing segmentation approaches for CT kidney and MRI ankle bone respectively. Both approaches are based on hierarchical ASM frameworks respectively (Erdt et al., 2010; Steger et al., 2014). Dice Similarity Coefficient DSC, Hausdorff Distance HD, and Volumetric Similarity VS are used as quality measures, whereas DSC and VS are listed in percent (larger values indicate better performance) and HD is given in millimeters (smaller values indicate better performance). We utilize the framework presented in (Erdt et al., 2010) for kidney segmentation which is driven primarily by an

Table 5: Reconstruction errors (mm) of ankle bones for different methods and degrees of incompleteness. The star $*$ indicates a statistically significant difference between the corresponding results and our method at a significance level $\alpha = 0.01$.

	0%	10%	20%	30%	40%	50%
PCA	**1.567 ± 0.295**	5.845 ± 0.357*	10.110 ± 1.055*	13.724 ± 1.804*	16.403 ± 2.266*	22.666 ± 3.646*
RPCA	1.811 ± 0.623*	**2.740 ± 0.991**	6.114 ± 1.285*	9.812 ± 2.547*	14.516 ± 3.132*	19.351 ± 2.126*
KPCA	5.709 ± 4.594*	7.023 ± 4.453*	10.496 ± 4.171*	14.290 ± 3.737*	17.018 ± 3.566*	20.296 ± 3.470*
NIPS-09	3.567 ± 1.891*	6.013 ± 2.345*	9.897 ± 1.487*	13.833 ± 2.157*	16.454 ± 2.754*	19.491 ± 2.460*
MICCAI-17	3.409 ± 0.871*	5.658 ± 1.806*	8.338 ± 2.567*	9.614 ± 2.036*	11.096 ± 3.780*	17.697 ± 2.960*
RKPCA	1.663 ± 0.196	3.528 ± 1.502	**5.981 ± 1.563**	**7.544 ± 2.268**	**9.762 ± 3.039**	**14.950 ± 2.953**

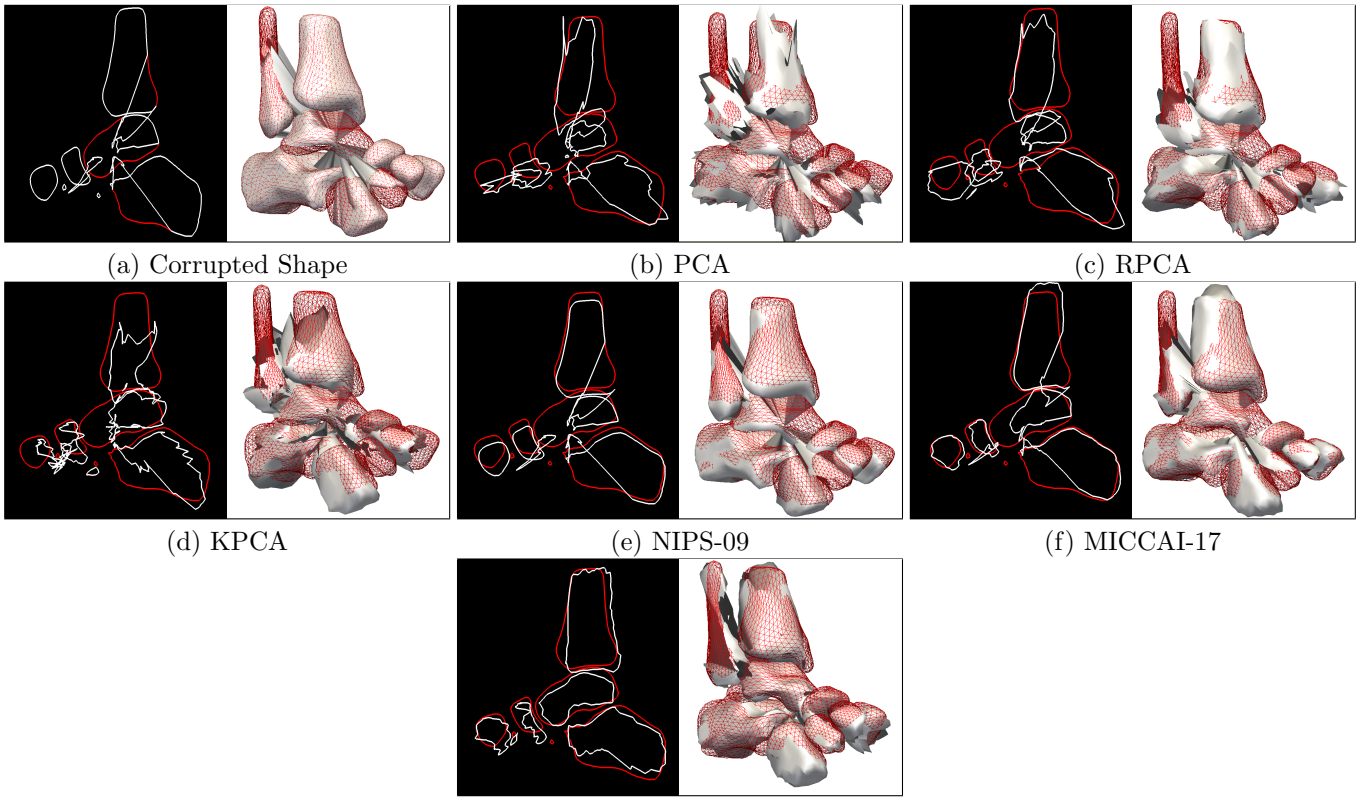

(a) Corrupted Shape (b) PCA (c) RPCA

(d) KPCA (e) NIPS-09 (f) MICCAI-17

(g) RKPCA

Figure 7: The figure plots an incomplete ankle bone shape (a) with its reconstructions from competitive models (b) - (g) illustrated from the perspective of Coronal-Axial view (left) and 3D rendering (right), where the red shape indicates the ground truth. (a) is artificially generated with 30% of pieces randomly removed.

automatic adaption to local intensity features and a global shape model back projection. In Table 6 we report the segmentation results using the competitive models. Our approach outperforms the other models in all measures.

We utilize the same ankle bone segmentation approach presented in (Steger et al., 2014) as in our previous conference work (Ma et al., 2017) and report results in Table 7. Our proposed model delivers an improvement from the previous work MICCAI-17 as well as other competitive approaches. Fig. 12 illustrates a segmentation result and several conclusions can be drawn from the segmentation results: (1) The overlap and abnormal deformation often occur in the area of the narrow inner space between each pair of sub-bones due to the poor image adaption, whereas our model effectively alleviates such corruption; (2) RPCA model often results in a smooth shape (cf. Fig. 7-(b)) where the discriminative features on the boundary are removed, this is mainly because that RPCA only preserves the high-frequency data but penalize the low-frequencies by the l_1 norm; (3) generally the nonlinear models outperform the linear models, however, the KPCA model shows worse performance in Table 7 compared to the RPCA model because KPCA is not robust to the corruption.

5. Discussion and Conclusion

In this work, we propose a novel Robust Kernel Principal Component Analysis approach for statistical shape

Table 6: Kidney Segmentation Results

	DSC			HD (mm)			VS		
	Mean	Min	Max	Mean	Min	Max	Mean	Min	Max
PCA	0.761±0.144	0.303	0.961	15.063±7.536	4.898	38.131	0.932±0.080	0.595	0.991
RPCA	0.802±0.064	0.608	**0.965**	15.962±7.198	**4.015**	35.818	0.942±0.060	0.620	0.990
KPCA	0.816±0.093	0.559	0.901	14.982±8.825	4.434	39.824	0.949±0.062	0.688	0.993
NIPS-09	0.821±0.083	0.519	0.955	14.074±6.417	5.385	32.802	0.953 ±0.049	0.811	**0.997**
MICCAI-17	0.863±0.086	0.570	0.960	13.664±8.320	5.385	36.576	0.968±0.071	0.707	0.995
RKPCA	**0.905±0.016**	**0.876**	0.945	**7.845±1.676**	5.099	**11.180**	**0.970±0.018**	**0.917**	0.994

Table 7: Ankle Bone Segmentation Results

	DSC			HD (mm)			VS		
	Mean	Min	Max	Mean	Min	Max	Mean	Min	Max
PCA	0.827±0.110	0.596	0.931	9.029±2.454	4.735	16.572	0.852±0.099	0.717	0.953
RPCA	0.863±0.031	0.796	0.952	8.432±2.925	3.021	17.203	0.902±0.034	0.807	0.978
KPCA	0.843±0.038	0.789	0.923	9.018±2.959	3.650	16.698	0.892±0.059	0.797	0.967
NIPS-09	0.872±0.016	0.841	0.944	8.398±2.265	2.960	14.021	0.918±0.057	0.791	0.979
MICCAI-17	0.908±0.033	0.825	0.960	7.881±2.210	4.361	13.210	0.940±0.030	0.886	0.990
RKPCA	**0.930±0.025**	**0.880**	**0.972**	**6.115±2.360**	**2.280**	**10.753**	**0.980±0.035**	**0.894**	**0.997**

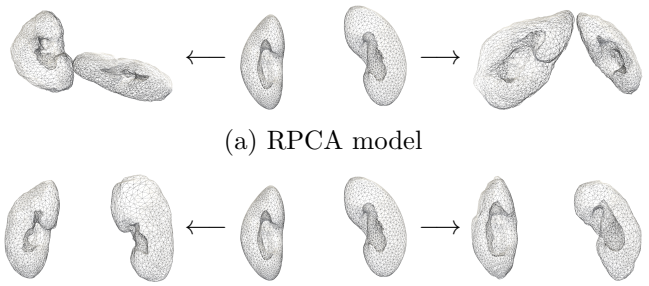

(a) RPCA model

(b) RKPCA model

Figure 8: The variance for the RPCA and RKPCA model, where the shape in the middle is the mean and the left and right shapes are generated from $-3\sqrt{\Lambda_1}$ and $+3\sqrt{\Lambda_1}$ for RPCA model, and $-\sqrt{N_s\Lambda_1}$ and $+\sqrt{N_s\Lambda_1}$ for RKPCA model respectively, with other modes set to the 0.

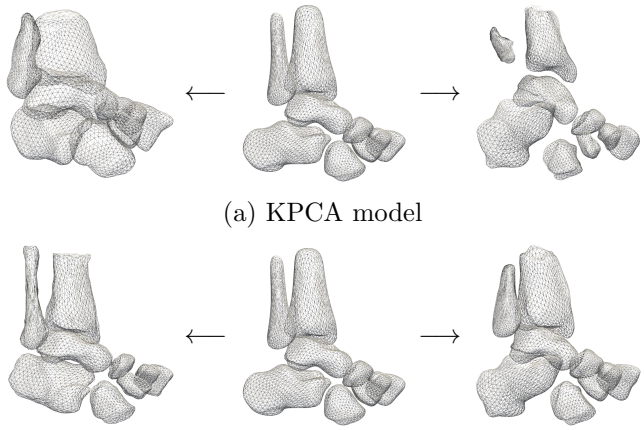

(a) KPCA model

(b) RKPCA model

Figure 9: The variance for the KPCA and RKPCA model, where the shape in the middle is the mean and the left and right shapes are generated from $-\sqrt{N_s\Lambda_1}$ and $+\sqrt{N_s\Lambda_1}$ for the first mode, with other modes set to 0.

modeling with the aim to derive an SSM that is robust to arbitrarily corrupted data and capable to model both linear and non-linear variabilities. Experiments are conducted on 30 public CT kidney pair volumes to validate the models' capability of representing non-linear features. Furthermore, 49 MRI ankle bones are used to validate the models' capability of handling highly corrupted data. To investigate the ability for arbitrary outlier recovery, we artificially generate corrupted datasets by removing a certain proportion of landmarks and measure the distance between its reconstructions from competitive models and ground truth afterwards. Experimental results show a significant advantage of our RKPCA in coping with arbitrary outliers. Moreover, we define an SSM with good quality that achieves a balance of the generalization ability and specificity (Davies et al., 2008). Even though the generalization ability for the PCA, RPCA kidney models is smaller than that of our proposed model, the specificity of our model is significantly smaller than the linear models. Besides, our models compactness performs better than that of the others. Hence, we argue that our proposed model outperforms the state-of-the-art models in terms of the relevant measures. Furthermore, the application of our model in segmentation frameworks also demonstrates higher accuracy in comparison to state of the art SSMs.

In addition to the application in statistical shape modeling, our proposed RPCA can also be used in other com-

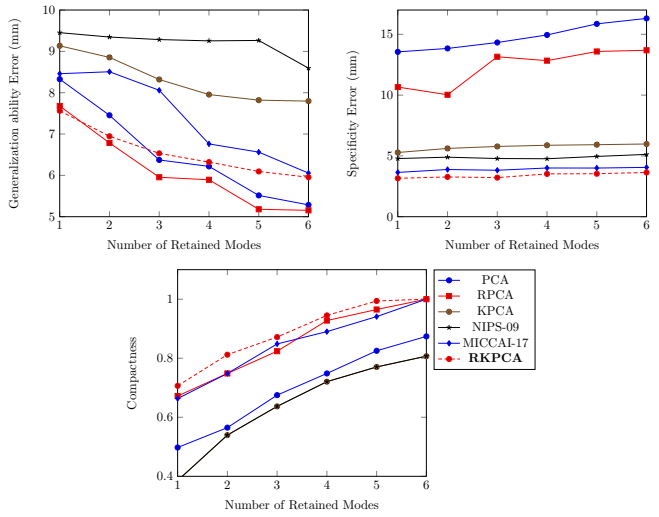

Figure 10: Generalization ability G, specificity S and compactness C for the kidney models.

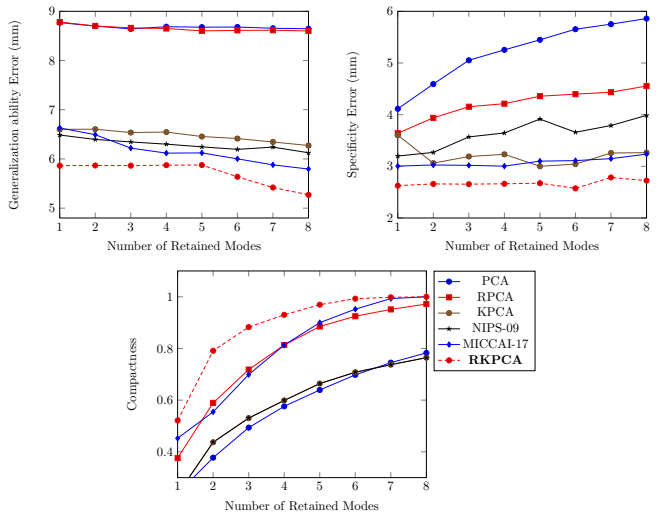

Figure 11: Generalization ability G, specificity S and compactness C for the ankle bone models.

pressive sensing areas, e.g. image and signal denoising, as it is capable to capture significant nonlinear patterns from any data matrix and it is robust to arbitrary outliers as well.

Several limitations do exist in practice, though. Generally, the training data needs to sufficiently cover the shape variances of the target object, i.e. as with other statistical shape modeling approaches, any abnormal shape not contained in the training data will not be modeled correctly. For example, for unhealthy organs with strong deformations or large tumors, RKPCA's robustness to corruptions may falsely try to correct these abnormalities. The same applies for significant articulated joint motions which are not present in the training data. On the other hand, the generalization ability and compactness of the models need to be explained more. Refer to Fig. 10, our RKPCA model lacks the generalization ability when the training datasets are free of outliers compared to the RPCA model. If it comes to modeling of normally distributed training data, RKPCA does not provide major advantages other than speed in comparison to KPCA. It is worth clarifying that a model is more general does not mean that it has more ability to handle the corrupted training data. Since we define a model with good quality achieves a balance of the generalization ability and specificity, our model still has high quality than the others as a whole. Besides, as the RKPCA model preserves 6 and 8 modes for the kidney pairs and ankle bones respectively (cf. Fig. 10 and Fig. 11), we only compare the first 6 and 8 modes for all the models. Moreover, SSMs are generally sensitive to initialization and RKPCA is no exception. It might be a problem even for large objects, e.g. the liver (Erdt et al., 2010; Norajitra and Maier-Hein, 2017). In this work, though, the initialization does not significantly degrade the segmentation accuracy. Still, this motivates us to combine our RKPCA with other approaches like deep neural networks to provide an accurate initialization method in future work, especially for small and highly deformable structures. In addition, since our method is an unsupervised training algorithm, the reconstruction from the model is not guaranteed to be exactly the same as the ground truth. To obtain a higher quality reconstruction in segmentation, in the future work, we may incorporate some prior knowledge such as partial label of the shape to make the reconstruction closer to the ground truth.

Acknowledgments

This research is supported by the National Research Foundation, Prime Minister's Office, Singapore under its International Research Centres in Singapore Funding Initiative. This work is partially supported by a grant AcRF RGC 2017-T1-001-053 by Ministry of Education, Singapore.

Albà, X., Pereañez, M., Hoogendoorn, C., Swift, A. J., Wild, J. M., Frangi, A. F. and Lekadir, K. (2016), 'An algorithm for the segmentation of highly abnormal hearts using a generic statistical shape model', *IEEE transactions on medical imaging* **35**(3), 845–859.

Anaraki, F. P. and Hughes, S. M. (2013), Kernel compressive sensing, *in* 'Image Processing (ICIP), 2013 20th IEEE International Conference on', IEEE, pp. 494–498.

Anas, E. M. A., Rasoulian, A., Seitel, A., Darras, K., Wilson, D., John, P. S., Pichora, D., Mousavi, P., Rohling, R. and Abolmaesumi, P. (2016), 'Automatic Segmentation of Wrist Bones in CT Using a Statistical Wrist Shape $+ $ Pose Model', *IEEE transactions on medical imaging* **35**(8), 1789–1801.

Cai, J.-F., Candès, E. J. and Shen, Z. (2010), 'A singular value thresholding algorithm for matrix completion', *SIAM Journal on Optimization* **20**(4), 1956–1982.

Candès, E. J., Li, X., Ma, Y. and Wright, J. (2011), 'Robust principal component analysis?', *Journal of the ACM (JACM)* **58**(3), 11.

Candès, E. J. and Recht, B. (2009), 'Exact matrix completion via convex optimization', *Foundations of Computational mathematics* **9**(6), 717.

Castro-Mateos, I., Pozo, J. M., Pereañez, M., Lekadir, K., Lazary, A. and Frangi, A. F. (2015), 'Statistical interspace models (SIMs):

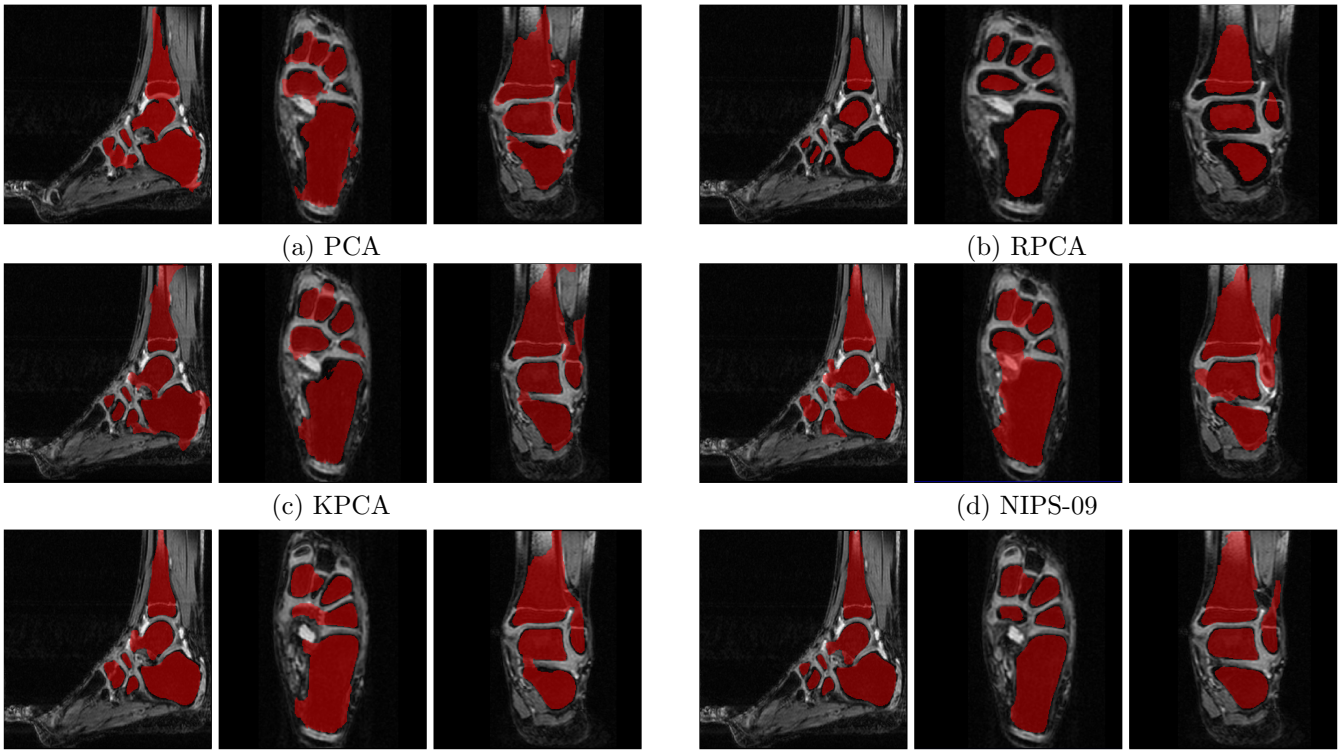

(a) PCA (b) RPCA (c) KPCA (d) NIPS-09 (e) MICCAI-17 (f) RKPCA

Figure 12: Comparisons of ankle bone segmentation results.

Application to robust 3D spine segmentation', *IEEE transactions on medical imaging* **34**(8), 1663–1675.

Chen, X., Graham, J., Hutchinson, C. and Muir, L. (2014), 'Automatic generation of statistical pose and shape models for articulated joints', *IEEE transactions on medical imaging* **33**(2), 372–383.

Davies, R., Twining, C. and Taylor, C. (2008), *Statistical models of shape: Optimisation and evaluation*, Springer Science & Business Media.

Erdt, M., Kirschner, M., Steger, S. and Wesarg, S. (2010), Fast automatic liver segmentation combining learned shape priors with observed shape deviation, *in* 'Computer-Based Medical Systems (CBMS), 2010 IEEE 23rd International Symposium on', IEEE, pp. 249–254.

Gutierrez, B., Mateus, D., Shiban, E., Meyer, B., Lehmberg, J. and Navab, N. (2014), A sparse approach to build shape models with routine clinical data, *in* 'Biomedical Imaging (ISBI), 2014 IEEE 11th International Symposium on', IEEE, pp. 258–261.

Heimann, T. and Meinzer, H.-P. (2009), 'Statistical shape models for 3D medical image segmentation: a review', *Medical image analysis* **13**(4), 543–563.

Kirschner, M., Becker, M. and Wesarg, S. (2011), 3D active shape model segmentation with nonlinear shape priors, *in* 'International Conference on Medical Image Computing and Computer-Assisted Intervention', Springer, pp. 492–499.

Kirschner, M. and Wesarg, S. (2010), Construction of Groupwise Consistent Shape Parameterizations by Propagation, *in* 'Proc. SPIE Medical Imaging 2010: Image Processing'.

Kwak, N. (2013), 'Nonlinear projection trick in kernel methods: An alternative to the kernel trick', *IEEE transactions on neural networks and learning systems* **24**(12), 2113–2119.

Landman, B., Xu, Z., Eugenio Igelsias, J., Styner, M., Robin Langerak, T. and Klein (eds), A. (n.d.), 2015 MICCAI Multi-Atlas Labeling Beyond the Cranial Vault - Workshop and Challenge, doi:10.7303/syn3193805.

Lin, Z., Chen, M. and Ma, Y. (2010), 'The augmented lagrange multiplier method for exact recovery of corrupted low-rank matrices', *arXiv preprint arXiv:1009.5055* .

Lüthi, M., Albrecht, T. and Vetter, T. (2009), Building shape models from lousy data, *in* 'International Conference on Medical Image Computing and Computer-Assisted Intervention', Springer, pp. 1–8.

Ma, J., Lin, F., Honsdorf, J., Lentzen, K., Wesarg, S. and Erdt, M. (2016), Weighted Robust PCA for statistical shape modeling, *in* 'Lecture Notes in Computer Science (including subseries Lecture Notes in Artificial Intelligence and Lecture Notes in Bioinformatics)', Vol. 9805 LNCS.

Ma, J., Lin, F., Wesarg, S. and Erdt, M. (2018), A novel bayesian model incorporating deep neural network and statistical shape model for pancreas segmentation, *in* 'International Conference on Medical Image Computing and Computer-Assisted Intervention', Springer, pp. 480–487.

Ma, J., Wang, A., Lin, F., Wesarg, S. and Erdt, M. (2017), Nonlinear statistical shape modeling for ankle bone segmentation using a novel kernelized Robust PCA, *in* 'Lecture Notes in Computer Science (including subseries Lecture Notes in Artificial Intelligence and Lecture Notes in Bioinformatics)', Vol. 10433 LNCS.

Mika, S., Schölkopf, B., Smola, A. J., Müller, K.-R., Scholz, M. and Rätsch, G. (1999), Kernel PCA and de-noising in feature spaces, *in* 'Advances in neural information processing systems', pp. 536–542.

Nguyen, H., Yang, W., Shen, F. and Sun, C. (2015), 'Kernel low-rank representation for face recognition', *Neurocomputing* **155**, 32–42.

Nguyen, M. H. and Torre, F. (2009), Robust kernel principal component analysis, *in* 'Advances in Neural Information Processing Systems', pp. 1185–1192.

Norajitra, T. and Maier-Hein, K. H. (2017), '3d statistical shape models incorporating landmark-wise random regression forests for omni-directional landmark detection', *IEEE transactions on medical imaging* **36**(1), 155–168.

Okada, T., Linguraru, M. G., Hori, M., Summers, R. M., Tomiyama, N. and Sato, Y. (2015), 'Abdominal multi-organ segmentation

from CT images using conditional shape–location and unsupervised intensity priors', *Medical image analysis* **26**(1), 1–18.

Patenaude, B., Smith, S. M., Kennedy, D. N. and Jenkinson, M. (2011), 'A Bayesian model of shape and appearance for subcortical brain segmentation', *Neuroimage* **56**(3), 907–922.

Pereañez, M., Lekadir, K., Castro-Mateos, I., Pozo, J. M., Lazáry, Á. and Frangi, A. F. (2015), 'Accurate segmentation of vertebral bodies and processes using statistical shape decomposition and conditional models', *IEEE transactions on medical imaging* **34**(8), 1627–1639.

Qi, H. and Hughes, S. (2011), Using the kernel trick in compressive sensing: Accurate signal recovery from fewer measurements, *in* 'Acoustics, Speech and Signal Processing (ICASSP), 2011 IEEE International Conference on', IEEE, pp. 3940–3943.

Rasoulian, A., Rohling, R. and Abolmaesumi, P. (2013), 'Lumbar spine segmentation using a statistical multi-vertebrae anatomical shape+ pose model', *IEEE transactions on medical imaging* **32**(10), 1890–1900.

Recht, B., Fazel, M. and Parrilo, P. A. (2010), 'Guaranteed minimum-rank solutions of linear matrix equations via nuclear norm minimization', *SIAM review* **52**(3), 471–501.

Shi, C., Cheng, Y., Wang, J., Wang, Y., Mori, K. and Tamura, S. (2017), 'Low-rank and sparse decomposition based shape model and probabilistic atlas for automatic pathological organ segmentation', *Medical image analysis* **38**, 30–49.

Soliman, A., Khalifa, F., Elnakib, A., El-Ghar, M. A., Dunlap, N., Wang, B., Gimel'farb, G., Keynton, R. and El-Baz, A. (2017), 'Accurate lungs segmentation on CT chest images by adaptive appearance-guided shape modeling', *IEEE transactions on medical imaging* **36**(1), 263–276.

Steger, S., Jung, F. and Wesarg, S. (2014), Personalized articulated atlas with a dynamic adaptation strategy for bone segmentation in CT or CT/MR head and neck images, *in* 'Medical Imaging 2014: Image Processing', Vol. 9034, International Society for Optics and Photonics, p. 90341I.

Sun, S., Bauer, C. and Beichel, R. (2012), 'Automated 3-D segmentation of lungs with lung cancer in CT data using a novel robust active shape model approach', *IEEE transactions on medical imaging* **31**(2), 449–460.

Twining, C. J. and Taylor, C. J. (2001), Kernel principal component analysis and the construction of non-linear active shape models., *in* 'BMVC', Vol. 1, pp. 23–32.

von Tycowicz, C., Ambellan, F., Mukhopadhyay, A. and Zachow, S. (2018), 'An efficient Riemannian statistical shape model using differential coordinates: With application to the classification of data from the Osteoarthritis Initiative', *Medical image analysis* **43**, 1–9.

Wilms, M., Ehrhardt, J. and Handels, H. (2012), A 4D statistical shape model for automated segmentation of lungs with large tumors, *in* 'International Conference on Medical Image Computing and Computer-Assisted Intervention', Springer, pp. 347–354.

Wilms, M., Handels, H. and Ehrhardt, J. (2017), 'Multi-resolution multi-object statistical shape models based on the locality assumption', *Medical image analysis* **38**, 17–29.

Wu, L. and Wang, Y. (2017), 'Robust hashing for multi-view data: Jointly learning low-rank kernelized similarity consensus and hash functions', *Image and Vision Computing* **57**, 58–66.

Xiao, S., Tan, M., Xu, D. and Dong, Z. Y. (2016), 'Robust kernel low-rank representation', *IEEE transactions on neural networks and learning systems* **27**(11), 2268–2281.

Zhang, L., Yang, T., Yi, J., Jin, R. and Zhou, Z.-H. (2016), Stochastic Optimization for Kernel PCA., *in* 'AAAI', pp. 2315–2322.